

Linear Polarization Demosaicking for Monochrome and Color Polarization Focal Plane Arrays

Simeng Qiu^{ID}, Qiang Fu^{ID}, Congli Wang^{ID}, Wolfgang Heidrich^{ID}

King Abdullah University of Science and Technology (KAUST), Saudi Arabia

simeng.qiu@kaust.edu.sa, qiang.fu@kaust.edu.sa, congli.wang@kaust.edu.sa, wolfgang.heidrich@kaust.edu.sa

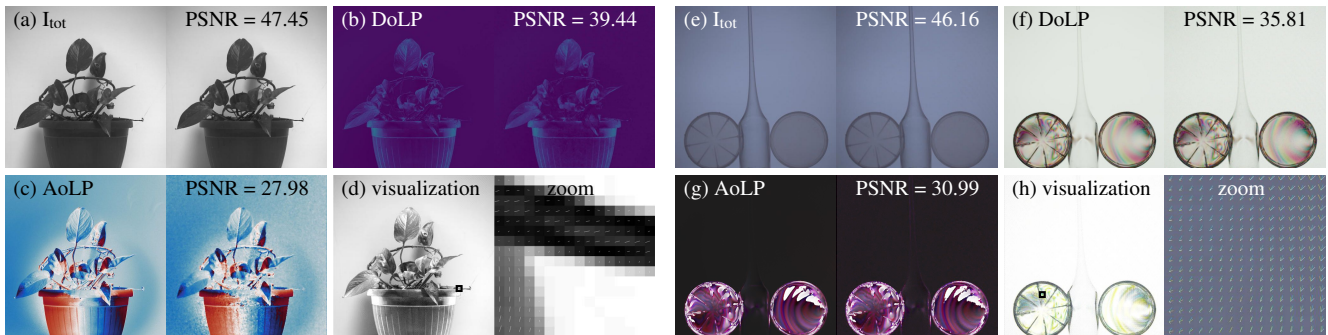


Figure 1: Left (a)-(d): Monochrome polarization demosaicking results for total intensity, DoLP, AoLP, and visualization with unpolarized illumination. Right (e)-(h): Color polarization demosaicking results for total intensity, DoLP, AoLP, and visualization with polarized illumination. Our proposed algorithm outperforms state-of-the-art for both monochrome and color polarization focal plane arrays.

Abstract

Division-of-focal-plane (DoFP) polarization image sensors allow for snapshot imaging of linear polarization effects with inexpensive and straightforward setups. However, conventional interpolation based image reconstruction methods for such sensors produce unreliable and noisy estimates of quantities such as degree of linear polarization (DoLP) or angle of linear polarization (AoLP). In this paper, we propose a polarization demosaicking algorithm by inverting the polarization image formation model for both monochrome and color DoFP cameras. Compared to previous interpolation methods, our approach can significantly reduce noise induced artifacts and drastically increase the accuracy in estimating polarization states. We evaluate and demonstrate the performance of the methods on a new high-resolution color polarization dataset. Simulation and experimental results show that the proposed reconstruction and analysis tools offer an effective solution to polarization imaging.

Keywords: polarization demosaicking, monochrome and color images, polarization camera, visualization

CCS Concepts

- Computing methodologies → Computational photography;

1. Introduction

Polarization is an important property of light in addition to its amplitude and phase. Polarization imaging has found uses in various disciplines and applications such as object inspection to detect stress, scratch recognition, shape detection for transparent objects. Other potential applications include 3D image reconstruction in microscopy, ranging in remote sensing. In nature, many diverse species have polarization sensitive vision systems, e.g., honeybees, mantis shrimps, etc. [Hor14]. Unfortunately, humans are incapable

of discerning polarization effects with the naked eye. To utilize polarization information in our daily life, a variety of polarization imaging, a.k.a imaging polarimetry techniques have been developed with the aid of various polarizing optical elements over the past few decades [TGCS06, AK02]. Nonetheless, high-resolution snapshot polarization imaging remains a significant challenge.

Recently a class of division-of-focal-plane (DoFP) image sensors have been developed, featuring compactness, non-moving parts, and a snapshot capture mode. In such cameras, a micro-

polarizer array with four polarization measurements is integrated into the pixels of the focal plane array sensor, similar to the way Bayer filters are integrated into color cameras [YMU^{*}16, GEM^{*}17, GDB^{*}18, HMB^{*}14]. Both monochrome and color versions of such DoFP polarization cameras are now commercially available. However, effective polarization reconstruction for such sensors remains a largely uninvestigated problem. As pointed out by Tibbs et al. [TDBR17, TDRB18], noise in the measurement may lead to significant artifacts and incorrect conclusions. We show a simple example in Figure 2 (b), where Gaussian noise with a standard deviation of 2 out of 255 is added in the measurement, and apparent artifacts arise on the edges in the Degree of Linear Polarization (DoLP) estimation by bilinear interpolation. This problem is even more severe for color polarization cameras since both polarization and color information need to be interpolated simultaneously and from sparser measurements.

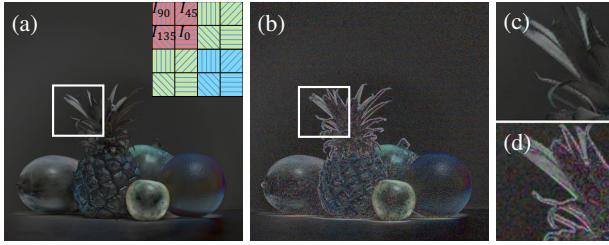


Figure 2: Noise induced artifacts in DoLP for bilinear interpolation in a color polarization camera. (a) Ground truth DoLP. (b) Reconstructed DoLP corrupted by noise (2 out of 255). The zoom regions (c) and (d) illustrate severe artifacts occurring at the edges using bilinear interpolation. The small figure in (a) is a micro-polarizer and Bayer filter layout for a color polarization camera.

To tackle polarization demosaicing problems, various interpolation methods have been proposed, e.g., bilinear, bicubic, cubic spline interpolation [GG11], Fourier domain demosaicing [TLR09], Intensity Correlation among Polarization Channels [ZLHC16], Sparse Representation-based Demosaicing [ZLL^{*}18], Newton’s Polynomial Interpolation [LZPK19], and End-to-end Fully-Convolutional Neural Network [ZLYY19]. We refer to the above methods for a complete summary. However, existing methods are tailored for monochrome polarization images, and distinct edge artifacts are prominent. Therefore, accurate numerical reconstruction from raw measurements for both monochrome and color polarization cameras other than the interpolation method is a must in practical applications.

This article is an extended version of [QFWH19], presented at VMV 2019. We present a high-quality reconstruction algorithm suitable for both monochrome and color polarization images at DOI: 10.5281/zenodo.4483248. A comprehensive image formation model by taking into account the Stokes vector conversion, micro-polarizer mosaicing, and noise model (Section 2) has been considered. We obtain significantly improved estimates of the intensity, Degree of Linear Polarization (DoLP), and Angle of Linear Polarization (AoLP) for monochromatic and color polarization images by solving an inverse problem within the alternating direction method of multipliers (ADMM) framework. Considering a high-

quality large polarization image dataset is lacking in this area, we construct a new dataset with 40 scenes (Section 3), including both unpolarized and polarized background illumination cases. This carefully captured high-resolution dataset covers a variety of polarization scenarios that are commonly seen in the real world, and we make it public for future research at DOI:10.25781/KAUST-2VA2X.

In addition to these contributions, in this article we extend [QFWH19] by providing new visualization methods for representing high-dimensional color+polarization imagery (Section 4). It is essential to visualize DoLP and AoLP individually as well as the polarization states as an entirety, and we present four visualization methods to complement conventional visualization approaches. We evaluate our algorithm on the polarization dataset and show numerical comparisons against the latest monochromatic and color polarization demosaicing methods. Experimental are carried out on real and simulated data to show that the proposed reconstruction method offers an effective solution to polarization imaging.

2. Polarization Demosaicking

2.1. Polarization Model

The Stokes vector describes the polarization states for incoherent illumination. In the case of linear polarization, we only consider the first three components of the Stokes vector, which are defined as

$$\mathbf{S} = \begin{bmatrix} S_0 \\ S_1 \\ S_2 \end{bmatrix} = \begin{bmatrix} I_{\text{tot}} \\ I_{\text{tot}} \mathcal{P} \cos(2\phi) \\ I_{\text{tot}} \mathcal{P} \sin(2\phi) \end{bmatrix} = \begin{bmatrix} \frac{1}{2}(I_0 + I_{45} + I_{90} + I_{135}) \\ I_0 - I_{90} \\ I_{45} - I_{135} \end{bmatrix}, \quad (1)$$

where I_{tot} is the total intensity, \mathcal{P} is DoLP and ϕ is AoLP. The Stokes parameters S_0 , S_1 , and S_2 are measured by four intensities I_0 , I_{45} , I_{90} and I_{135} with linear polarizers oriented at 0° , 45° , 90° and 135° respectively. DoLP and AoLP are defined as

$$\mathcal{P} = \frac{\sqrt{S_1^2 + S_2^2}}{S_0}, \quad \phi = \frac{1}{2} \arctan\left(\frac{S_2}{S_1}\right), \quad (2)$$

The polarization state of light can be changed by introducing polarizing optical elements, e.g. polarizers and retarders into the optical path. This process can be written in matrix-vector form as

$$\mathbf{S}' = \mathbf{MS} = \begin{bmatrix} m_{11} & m_{12} & m_{13} \\ m_{21} & m_{22} & m_{23} \\ m_{31} & m_{32} & m_{33} \end{bmatrix} \mathbf{S}, \quad (3)$$

where $\mathbf{M} \in \mathbb{R}^{3 \times 3}$ is a Müller matrix for the polarizing optical element. The Müller matrix for a linear polarizer oriented at an angle of θ with respect to horizon can be expressed as Eq. (4). In reality, fabrication artifacts lead to imperfections on the polarizer. So we should add k_1 as the transmittance (major) parallel to the orientation angle and k_2 as the transmittance (minor) perpendicular to the orientation angle, where $0 \leq k_1, k_2 \leq 1$ (see Appendix A).

2.2. Image Formation Model

The essential quantities of polarization analysis are I_{tot} , DoLP, and AoLP. Since the Stokes vector as well as the DoLP and AoLP are highly non-linear functions of the raw sensor data, any noise gets amplified in the estimates for DoLP and AoLP. On the other hand, the formulas for the DoLP and AoLP (Eq. (2)) are also non-convex,

$$\mathbf{M}_\theta = \frac{1}{2} \begin{bmatrix} k_1 + k_2 & (k_1 - k_2) \cos(2\theta) & (k_1 - k_2) \sin(2\theta) \\ (k_1 - k_2) \cos(2\theta) & (k_1 + k_2) \cos^2(2\theta) + 2\sqrt{k_1 k_2} \sin^2(2\theta) & (k_1 + k_2 - 2\sqrt{k_1 k_2}) \sin(2\theta) \cos(2\theta) \\ (k_1 - k_2) \sin(2\theta) & (k_1 + k_2 - 2\sqrt{k_1 k_2}) \sin(2\theta) \cos(2\theta) & (k_1 + k_2) \sin^2(2\theta) + 2\sqrt{k_1 k_2} \cos^2(2\theta) \end{bmatrix}, \quad (4)$$

making it difficult to directly demosaic these channels. Instead, we propose to solve the Stokes vectors by modeling the physical image formation from Stokes to intensity. With a better estimation of the Stokes vector, higher accuracy in DoLP and AoLP can be obtained.

Most image sensors directly measure intensity values, which are just the first component of the Stokes vector. With polarization image sensors, there are however, four different types of pixels, which have polarization filters for $0^\circ, 45^\circ, 90^\circ$ and 135° , respectively. We can describe the measured raw values of such a sensor by a 4×3 matrix \mathbf{C} , in which each row corresponds to the first row of the Müller matrix for the corresponding polarization filter (Eq. (4)):

$$\mathbf{I} = \begin{bmatrix} I_0 \\ I_{45} \\ I_{90} \\ I_{135} \end{bmatrix} = \mathbf{CS} = \begin{bmatrix} m_{11}^0 & m_{12}^0 & m_{13}^0 \\ m_{11}^{45} & m_{12}^{45} & m_{13}^{45} \\ m_{11}^{90} & m_{12}^{90} & m_{13}^{90} \\ m_{11}^{135} & m_{12}^{135} & m_{13}^{135} \end{bmatrix} \mathbf{S}, \quad (5)$$

The captured color image is a mosaic of intensities filtered by the micro-polarizers, and also by Bayer filters in the color case. The color-polarization DoFP sensor we used has a 2×2 pixels (representing polarization at 4 angles) in each color channel according to the Bayer pattern (see inset in Fig. 2a), thus combining a set of 4×4 super-pixel, which is different from regular color sensor. However, in the monochrome case, only 2×2 pixels form a super-pixel, which only contains the 4 polarization angles. This can be represented by pixel-wise multiplications by the respective mosaic masks. Therefore, the polarization image formation model can be expressed as

$$\mathbf{y} = \mathbf{BKAs} + \mathbf{n}, \quad (6)$$

where $\mathbf{s} \in \mathbb{R}^{3cN}$ is the vector form of stacked unknown Stokes parameters for each pixel in each color channel c . For monochrome cameras, $c = 1$, and for RGB cameras, $c = 3$. The total number of sensor pixels is N . We first create a three-block diagonal matrix $\mathbf{A} \in \mathbb{R}^{4cN \times 3cN}$ that converts the unknown Stokes vectors to measured intensities at four degrees for each color channel, and each block matrix in \mathbf{A} is a \mathbf{C} matrix. Second, we construct a selection matrix $\mathbf{K} \in \mathbb{R}^{cN \times 4cN}$. \mathbf{K} picks specific vector components according to the specific 2×2 intensity pixel pattern for each color channel. Then we applied a selection matrix $\mathbf{B} \in \mathbb{R}^{N \times cN}$ to formulate a Bayer pattern according to the set of 4×4 super-pixel. For the monochrome camera, the Bayer filter diminishes, so $\mathbf{B} = \mathbb{I}$ becomes an identity matrix. Finally, we add Gaussian noise $\mathbf{n} \in \mathbb{R}^N$, and formulated a captured raw data $\mathbf{y} \in \mathbb{R}^N$.

2.3. Inverse Problem

To recover the unknown Stokes vectors, we solve a constrained optimization problem within the ADMM framework. This framework has been very successful in many image reconstruction tasks, including color image demosaicing [HST*14], especially when combined with sophisticated regularization terms such as a cross-channel prior [HRH*13], or BM3D denoising [DFKE07]. How-

ever, our experiments (see Sec. 5) show that many of these regularizers do not significantly improve reconstruction results for polarization images, and can in fact be detrimental to reconstruction quality. In other words, priors developed for color images do not necessarily hold for polarization images. Instead, our proposed polarization demosaicing method takes the simpler form

$$\begin{aligned} \underset{\mathbf{s}}{\text{minimize}} \quad & \frac{1}{2} \|\mathbf{y} - \mathbf{BKAs}\|_2^2 + \lambda_1 h(\mathbf{D}_1 \mathbf{s}) + \lambda_2 h(\mathbf{D}_2 \mathbf{s}), \\ \text{subject to} \quad & -1 \leq \mathbf{s}_1, \mathbf{s}_2 \leq 1, \\ & 0 \leq \mathbf{s}_0 \leq 2, \\ & |\mathbf{s}_1|, |\mathbf{s}_2| \leq \mathbf{s}_0, \end{aligned} \quad (7)$$

where the first term in Eq. (7) is a data fitting term, and the second and third terms are the regularizers, which represent Huber penalties on the derivatives of the Stokes vectors ($\mathbf{D}_1 \mathbf{s} = \nabla_1 \mathbf{s}$, $\mathbf{D}_2 \mathbf{s} = \nabla_2^2 \mathbf{s}$). The Huber penalty [Hub64] is

$$h(x) = \begin{cases} \frac{1}{2}x^2, & |x| \leq \delta, \\ \delta \left(|x| - \frac{1}{2}\delta \right), & |x| > \delta, \end{cases} \quad (8)$$

where δ is a parameter that determines the transition points. We adopt Huber penalty here because it overcomes the penalization of small gradients inherent to total variation (TV), and therefore improves the reconstruction of image gradients while still maintaining sharp edges. The constraints in Eq. (7) enforce physical properties of the individual components of the Stokes vector \mathbf{s} : assuming that the individual polarization measurements are normalized to the range $[0 \dots 1]$, then the total intensity \mathbf{s}_0 falls in the range $[0 \dots 2]$, while \mathbf{s}_1 and \mathbf{s}_2 range from -1 to 1 . Also, the absolute value of \mathbf{s}_1 and \mathbf{s}_2 are always less than or equal to \mathbf{s}_0 . These physical properties can be seen directly from the definition of the Stokes vector (1) and the DoLP/AoLP (2). Sensor noise and interpolation artefacts could result in violations of these physical constraints, so that explicit enforcement in the optimization method becomes necessary in order to avoid artefacts in the derived quantities DoLP and AoLP.

Within the ADMM framework, the problem is split into two subproblems and solved separately. We introduce two slack variables $\mathbf{z}_1 = \mathbf{D}_1 \mathbf{s}$ and $\mathbf{z}_2 = \mathbf{D}_2 \mathbf{s}$. In the \mathbf{s} -problem, we solve

$$\begin{aligned} \underset{\mathbf{s}}{\text{minimize}} \quad & \frac{1}{2} \|\mathbf{y} - \mathbf{BKAs}\|_2^2 + \lambda_1 \|\mathbf{D}_1 \mathbf{s}\|_h + \lambda_2 \|\mathbf{D}_2 \mathbf{s}\|_h, \\ \text{subject to} \quad & \mathbf{D}_1 \mathbf{s} = \mathbf{z}_1, \\ & \mathbf{D}_2 \mathbf{s} = \mathbf{z}_2, \end{aligned} \quad (9)$$

Eq. (9) is transformed into an unconstrained problem

$$\begin{aligned} \underset{\mathbf{s}}{\text{minimize}} \quad & \frac{1}{2} \|\mathbf{y} - \mathbf{BKAs}\|_2^2 + \lambda_1 \|\mathbf{z}_1\|_h + \frac{\rho_1}{2} \|\mathbf{z}_1 - \mathbf{D}_1 \mathbf{s} - \mathbf{u}_1\|_2^2 \\ & + \lambda_2 \|\mathbf{z}_2\|_h + \frac{\rho_2}{2} \|\mathbf{z}_2 - \mathbf{D}_2 \mathbf{s} - \mathbf{u}_2\|_2^2, \end{aligned} \quad (10)$$

Therefore, the individual update rules for \mathbf{s}^{n+1} , \mathbf{z}^{n+1} , and \mathbf{u}^{n+1} are as follows:

$$\begin{aligned}\mathbf{s}^{n+1} &= \underset{\mathbf{s}}{\operatorname{argmin}} \quad \frac{1}{2} \|\mathbf{y} - \mathbf{BKA}\mathbf{s}\|_2^2 + \frac{\rho_1}{2} \|\mathbf{z}_1^n - \mathbf{D}_1\mathbf{s} - \mathbf{u}_1^n\|_2^2 \\ &\quad + \frac{\rho_2}{2} \|\mathbf{z}_2^n - \mathbf{D}_2\mathbf{s} - \mathbf{u}_2^n\|_2^2,\end{aligned}\quad (11)$$

$$\mathbf{z}_{1/2}^{n+1} = \text{shrinkage}(\mathbf{D}_{1/2}\mathbf{s}^{n+1} + \mathbf{u}_{1/2}^n, \mathcal{S}_\delta(\mathbf{s}^{n+1})), \quad (12)$$

$$\mathbf{u}_{1/2}^{n+1} = \mathbf{u}_{1/2}^n + (\mathbf{D}_{1/2}\mathbf{s}^{n+1} - \mathbf{z}_{1/2}^{n+1}), \quad (13)$$

For solving optimal value of \mathbf{s}^{n+1} in Eq. (11), we first calculate its derivative

$$\begin{aligned}&(\mathbf{A}^T \mathbf{K}^T \mathbf{B}^T \mathbf{BKA} + \rho_1 \mathbf{D}_1^T \mathbf{D}_1 + \rho_2 \mathbf{D}_2^T \mathbf{D}_2) \mathbf{s}^{n+1} \\ &= \mathbf{A}^T \mathbf{K}^T \mathbf{B}^T \mathbf{y} + \rho_1 \mathbf{D}_1^T (\mathbf{z}_1^n - \mathbf{u}_1^n) + \rho_2 \mathbf{D}_2^T (\mathbf{z}_2^n - \mathbf{u}_2^n),\end{aligned}\quad (14)$$

After derivation, the updated \mathbf{s}^{n+1} then is solved efficiently by a Conjugate Gradient solver, and the \mathcal{S}_δ is the well-known soft shrinkage:

$$\mathcal{S}_\delta(\mathbf{s}) = \begin{cases} \frac{\rho}{\lambda + \rho} \mathbf{s}, & |\mathbf{s}| \leq \left(1 + \frac{\lambda}{\rho}\right) \delta, \\ \mathbf{s} - \frac{\delta}{\rho}, & \mathbf{s} > \left(1 + \frac{\lambda}{\rho}\right) \delta, \\ \mathbf{s} + \frac{\delta}{\rho}, & \mathbf{s} < -\left(1 + \frac{\lambda}{\rho}\right) \delta. \end{cases} \quad (15)$$

3. Polarization Image Dataset

Systematic evaluation of our demosaicking method and competing techniques requires a realistic, high quality test dataset with ground truth results. To the best of our knowledge, existing polarization image datasets are monochromatic, and consist of only a few scenes [LGFB18, TDRB18]. High-resolution polarization images with color, are lacking for research. Therefore, we construct a polarization image dataset containing 40 carefully calibrated ground truth images with a wide range of scenes. We try to cover as many naturally occurring polarization effects as possible. We capture different scenes with various shapes, materials, and lighting conditions. In particular, polarized illumination is an essential and useful phenomenon in artifact diagnosis and industrial inspection. We include such images by capturing transparent objects in front of a highly polarized monitor. Figure 3 is a gallery of our polarization image datasets.

The dataset is captured by the division-of-time (DoT) strategy. We use a FLIR Grasshopper3 GS3-U3-41C6C color camera. The sensor is a CMOSIS CMV4000-3E5 CMOS, with 2048×2048 pixels. Each pixel is $5.5\mu\text{m} \times 5.5\mu\text{m}$. A Canon EF50mm f/1.8 II lens is used at its maximum aperture size. We mount a linear wire grid polarizer (WP25M-VIS, Thorlabs) on a high-resolution rotary stage (T-RSW60A, Zaber), and place it in front of the camera. The linear polarizer has more than 800 : 1 extinction ratio over the visible spectrum from 420nm to 700nm . For each scene, we capture four groups of raw images at 0° , 45° , 90° and 135° with the same exposure time. Each group has 100 images captured consecutively. We take the average of these 100 images to suppress noise. We also do a 2×2 pixel binning in the averaged image to further increase

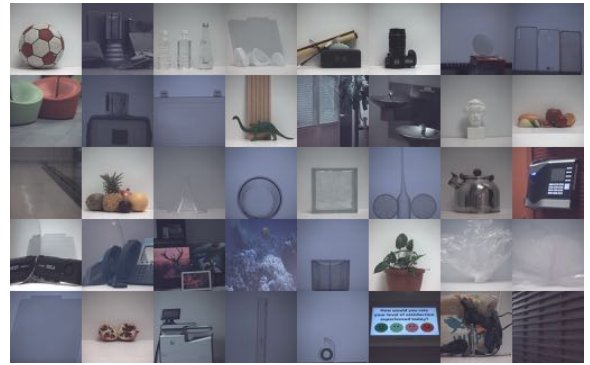


Figure 3: Gallery of our polarization image dataset. Only intensity components are shown here. The complete dataset is available at DOI:10.25781/KAUST-2VA2X.

the signal-to-noise ratio. With such pre-processing, we can generate high-quality ground truth data for I_{tot} , DoLP, and AoLP.

4. Color Polarization Image Visualization



Figure 4: We show the intensity component, DoLP in sRGB color space, AoLP, and 9D polarization visualization.

In addition to providing quantitative numerical results for experiments, it is also useful to visually analyze image results. In the case of color polarization images, this is made complicated by the high dimensionality of the data, with a total of 9 channels. Representing this data in a single image is a challenging task. We therefore explore both individual visualizations of DoLP and AoLP as well as an integrated visualization of all polarization states in their entirety. We proposed the following visualization methods to complement existing approaches. Figure 4 shows our visualization results for two typical scenarios. The top row is a natural scene with indoor illumination. The bottom scene with highly linear polarization illumination in the background.

4.1. Degree of Linear Polarization

A straightforward way to visualize the DoLPs for each color channel is to map the DoLP values to a color map and display the false color image separately, with a color bar indicating the values in DoLPs. Figure 5 shows this method for the above two scenes. Here we adopt the viridis color map. While this method presents all the

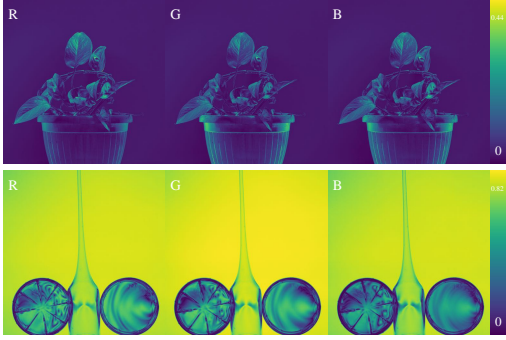


Figure 5: Visualization of DoLP by false color images. DoLP values are projected to a false color image.

relevant data, it is very hard to visually make out any color dependencies in the polarization state.

Since the valid data for DoLP is linear in the range between 0 and 1, we can concatenate the respective DoLPs in its corresponding color channel, and convert it to a color image in the sRGB color space, as shown in the second column in Figure 4. If there is no difference of DoLPs between color channels, the color would appear gray and the level of gray indicates the values of DoLPs. Perceptually, a white in this DoLP image indicates complete linear polarization, while black corresponds to a complete lack of polarization. The plant scene in Figure 4 illustrates this effect. The background is nearly unpolarized, so it appears dark. Reflection induced polarization on parts of the leaves has higher DoLP, and looks brighter than others. There is little DoLP difference between color channels, hence the overall DoLP image looks gray.

For the bottom row of Figure 4, the background illumination from a computer monitor is strongly linearly polarized, so it appears much brighter. Significant differences in DoLP across color channels lead to color fringes in the plastic wafer carriers because of internal stress. The appearance of color reflects which color channel(s) has larger DoLP values. For example, red means the DoLP is larger than those in the green and blue channels. Such effects can hardly be seen in the corresponding intensity image.

4.2. Angle of Linear Polarization

The valid range for AoLP is $[0^\circ, 180^\circ]$, but the cyclic nature of angles leads to a wraparound at 180° , which is essentially the same as 0° . Direct mapping from angle values to gray levels, as shown in the third column in Figure 4, may lead to misinterpretation for AoLPs that are close to 0° or 180° . Usually the noisy patterns occur in the AoLPs when there is a large difference between color channels due to angle wraparounds. Thereby it is more reasonable to look at the difference of AoLPs by considering the wraparound. We propose to take the AoLP in green channel as a reference, and calculate the absolute difference in blue and red channels with respect to green. To compensate the angle wraparounds, we calculate the AoLP difference in the following way

$$\Delta\phi_i = \min(|\phi_i - \phi_{\text{ref}}|, 180^\circ - |\phi_i - \phi_{\text{ref}}|), \quad (16)$$

where i is either blue or red, and the reference here is green.

We show various visualizations of AoLP in Figure 6 for the

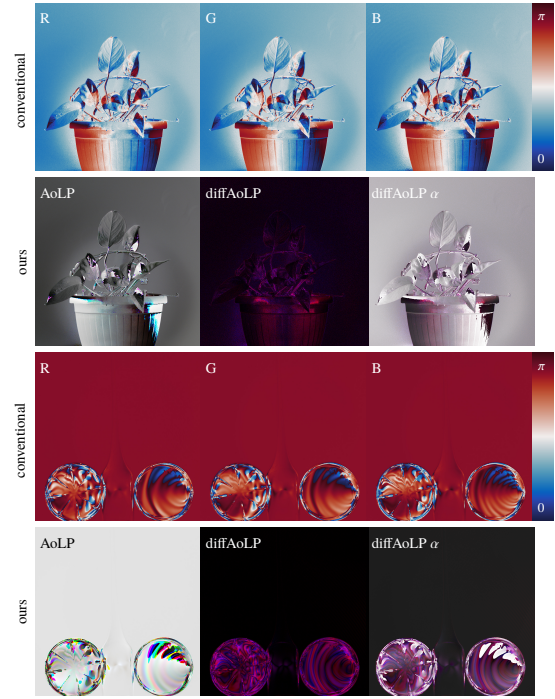


Figure 6: Visualization of AoLP in three ways. From left to right.

above two scenes. The first and third rows are the conventional way to display AoLP in false color with a color bar. We adopt the cmocean “balance” color map here. The second and fourth rows show our visualization methods in three ways. The first way is to cast normalized AoLP values into their corresponding color channels. This is shown in the third column in Figure 4 as well as in the first column in Figure 6. The gray levels indicate the values of AoLP. If there is significant difference of AoLPs among color channels, color fringes show up, and the color indicates which color channel(s) has larger AoLP values. The second visualization is to show difference AoLP (diffAoLP) as a color image. We take the green channel as a reference, because the sensor response in green is higher than the other two, and hence the AoLP is more reliable in this channel. The absolute difference AoLP values are cast into red and blue channels accordingly. The larger the relative difference, the more prominent the color in the corresponding channel(s) in the diffAoLP image. The third approach is to mitigate the fact that in some cases where diffAoLP is rather small and hardly visible. We set the green AoLP values as a transparency α channel to make it more visible, as shown in the third columns in Figure 6. Compared with the direct mapping visualization of AoLP in the first columns, the diffAoLP and diffAoLP α images reveal more comprehensive information. The paper, we use diffAoLP α for AoLP visualization.

4.3. Visualization in 9D

Although the above individual visualizations of DoLP and AoLP reflect the fine details of different aspects of polarization states, visualizing polarization as an entirety would be more helpful to interpret the whole picture of polarization states. This is particu-

larly reasonable when DoLP is rather small, since then the AoLP becomes arbitrary, and hence meaningless. The complete visualization of polarization states for color polarization images requires to show 9D data at the same time. In analogy to a vector field within a unit circle, the magnitude links to the value of DoLP, and the direction represents AoLP. Since the wraparound of AoLP happens at 180° , the upper and lower halves of the unit circle are centrosymmetric. Therefore, we can calculate the vector field as

$$(\mathbf{u}, \mathbf{v}) = (\mathcal{P} \cos(2\phi), \mathcal{P} \sin(2\phi)). \quad (17)$$

We propose to overlay the above vector fields on top of the total intensity component, which is essentially a color image. As shown in the fourth and fifth columns in Figure 4, we denote the vector fields with short lines in different colors. The length of the line reflects DoLP, and the orientation of the line indicates AoLP. The color scheme of the lines are chosen in order not to interfere with the original color, but still approximating it. We choose cyan for the blue channel, yellow for green, and white for red. This color scheme keeps the original color of the image very well, and “pops up” the regions with strong polarization. For small DoLPs, the vector field becomes a small dot, and hence negligible in area. The length and orientation differences among the vector fields indicate a noticeable difference of polarization states among color channels. In the glass and plastic scene, the vector fields exhibit different lengths and orientations among three color channels.

4.4. Virtual Polarizer

The above methods are developed for static images. In an interactive exploration tool, of course more options exist. Since the complete polarization information has been stored in total intensity, DoLP and AoLP, we can synthesize new intensity images with a temporally changing “virtual” polarizer as if the images were taken under the same physical conditions. A virtual linear polarizer can be fully modeled by the Müller matrix. Figure 7 shows intensity images with an ideal virtual linear polarizer oriented at different yet arbitrary angles. Note the slight brightness changes in the shiny areas on the plant leaves. The effect gets more obvious for the glass and plastic scene for the drastic changes of polarization states among color channels. For static images the effect is rather subtle, even in side-by side images, which prompted the development of the methods described above. Please refer to the Supplementary Video for a better experience of the virtual polarizer method. For a thorough review of the both conventional and proposed visualization methods, we show an unpolarized illumination of Figure 8.

5. Results

We first evaluate our algorithm by simulation on our polarization image dataset and then by real experiments to demonstrate the real performance. In the simulation, we compare our algorithm against state-of-the-art polarization demosaicing algorithms. The reconstruction quality is evaluated in terms of peak signal-to-noise ratio (PSNR) on three quantities: total intensity, DoLP, and AoLP.

5.1. Monochromatic Simulation Results

Conventional polarization demosaicing algorithms focus mainly on monochromatic images [MLB18]. State-of-the-art algorithms include bilinear, bicubic, bicubic spline interpolations [GG11],

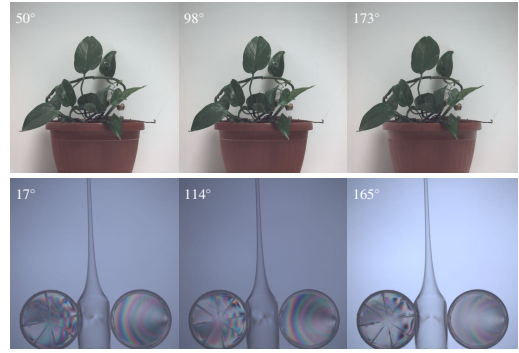


Figure 7: Synthetic intensity images: New intensity images are obtained by multiplying the known Stokes vectors by the Müller matrix and extract the new S_0 component.

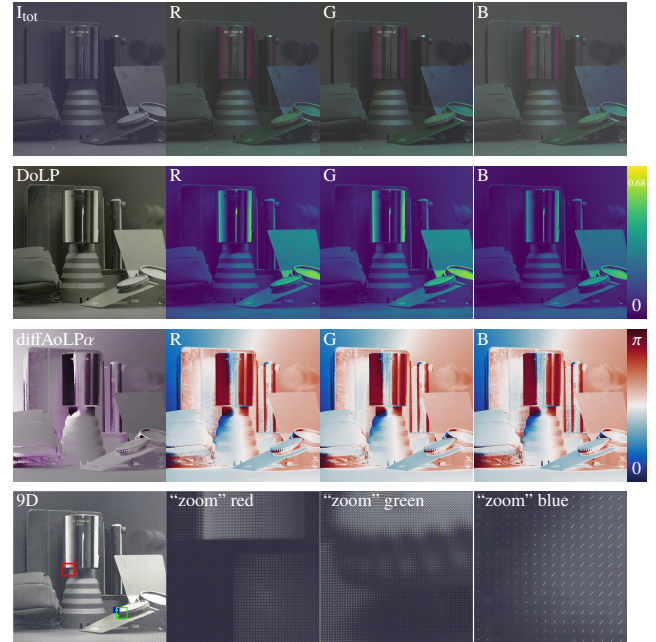


Figure 8: *blackstuff* scene: First row shows the false color image in HSV space. The second and third row show DoLP and AoLP in false color, and diffAoLP with transparency channel.

Fourier domain demosaicing [TLR09], Intensity Correlation among Polarization Channels (ICPC) [ZLHC16], Sparse Representation-based Demosaicing (SR) [ZLL*18], Newton’s Polynomial Interpolation (Newton) [LZPK19], and End-to-end Fully-Convolutional Neural Network (E2E) [ZLY19]. Therefore, we compare against these methods in the monochrome case. We take the green channel from our color polarization image dataset as the ground truth monochrome polarization data, because it has a better signal to noise ratio than the other two channels.

We show two exemplary results in Figure 9, a ball scene with unpolarized background illumination and a containers scene with polarized illumination. In both cases, we add Gaussian noise

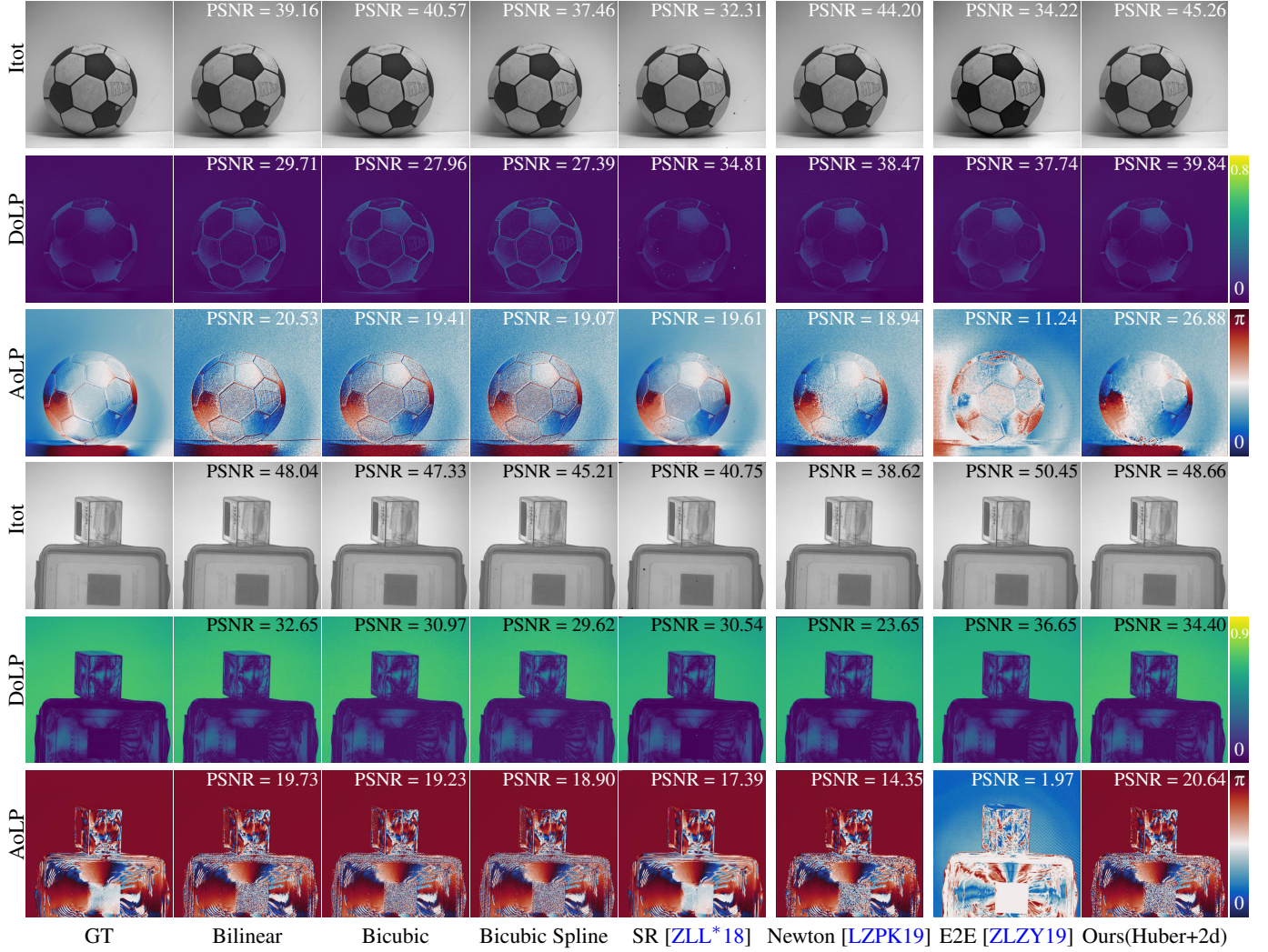


Figure 9: Monochromatic polarization demosaicking. The upper part is a ball scene with unpolarized illumination, and the low part is a containers scene with polarized illumination. The reconstruction quality is presented in PSNR for all the methods for comparison.

with standard deviation $\sigma = 2$. For conventional methods, there exist distinct edge artifacts because of interpolation, e.g., around the border between black and white patches on the ball. They tend to overestimate DoLP, while our method can suppress these artifacts. We quantitatively compare PSNRs for all the methods on the intensity, DoLP and AoLP. The results show our method performs significantly better in all the three polarization components.

The ICPC [ZLHC16] method claims to achieve better visual results than simpler interpolation methods, and the DoLP and intensity have lower root-mean-square error (RMSE) than bilinear, bicubic, and bicubic spline interpolation. However, running the ICPC method on our full dataset, we observe that although the intensity results of ICPC are almost always better than the other competitors, the DoLP results are not always higher than simple filtering. In particular, for the scenes with polarized illumination the reconstructed DoLP is quite low, as shown in the lower part of Figure 9.

In addition, ICPC does not account for AoLP in the reconstruction, resulting in poor AoLP results. Another competitive method, Fourier domain demosaicking [TLR09] is robust, but the DoLP is sometimes lower than bilinear and ICPC but overall higher than the other methods. The AoLP of Fourier domain demosaicking has the same situation with DoLP. In total, our method has better reconstruction quality.

It is worth noting that the range of DoLP is $[0, 1]$. However, existing methods tend to overestimate DoLP, so in dark regions these methods could have DoLP values larger than 1, which is physically impossible. This has been pointed out by Tibbs et al. [TDRB18].

Sparse Representation (SR) [ZLL*18] proposed by Zhang et al. is one of the representative approach for solving monochrome polarization demosaicking. However, the deficiency of this method is quite obvious on both Figures and PSNR results. In Figure 9 fifth column, there are missing pixels for each recovery parame-

Table 1: Average PSNR results through the whole dataset for monochromatic polarization demosaicking ($\sigma = 2$).

Average PSNR		Bilinear	Bicubic	Bicubic Spline	Fourier	ICPC	SR	Newton	E2E	Ours (Huber2d)
Unpolarized illumination	Itot	42.85	43.46	40.57	41.63	45.07	34.03	44.16	27.96	47.91
	DoLP	32.45	30.71	29.94	31.64	29.38	34.21	36.68	40.00	40.43
	AoLP	19.83	18.72	18.31	18.07	10.82	21.51	17.20	7.57	25.46
Polarized illumination	Itot	45.89	45.58	43.04	45.04	47.19	37.38	35.22	47.31	46.34
	DoLP	33.99	32.92	29.53	32.38	5.42	32.87	22.47	32.10	34.63
	AoLP	30.02	29.47	28.54	29.37	15.99	22.67	17.80	1.69	31.37

ter, and the PSNR for total intensities in Table 1 are lower than almost all the comparison methods. Another prevalent method is Newton’s polynomial interpolation (Newton) [LZPK19]. This approach is very efficiency and has excellent results on the unpolarized illumination scenes except for AoLP recovery. However, as shown in the polarized illumination, the recovery resolution is not comparable. An end-to-end fully-convolutional neural network (E2E) [ZLZY19] just published recently. We applied their best model with correct DoFP sensor pattern and test it on our proposed dataset. As shown in Figure 9, it is evident that AoLP approximation is not accurate, especially in polarized illumination. That may because the original training dataset from E2E [ZLZY19] fail to include polarized illumination scenes. However, for total intensity and DoLP recovery, polarized illumination has distinctive improvement, which are even better than our proposed method in containers scene. We run E2E method through our entire dataset and calculate the average PSNR results for three parameters. Their total intensity recovery in polarized scene is slightly better than ours. Although training data from E2E are purely unpolarized illumination, the reconstruction results for all the parameters are still lower than ours. Considering that various factors could affect polarization states, we run the comparison for all the methods on our entire dataset. The average PSNR results in Table 1, demonstrates the effectiveness and robustness of our method.

5.2. Color Simulation Results

Since both color and polarization information offers even more information about the scene, our work puts more focus on testing our algorithm on color polarization demosaicking. This brings much more challenges for the interpolation methods, because color and polarization are independent properties of light, and joint demosaicking of the two is difficult to reconstruct in the sense of *interpolation*. There are few algorithms for this purpose in the literature, so instead of comparing with interpolation based methods, we compare different priors/regularizers in our optimization framework.

Specifically, we consider candidate image priors commonly used in image reconstruction, including total variation on first order derivatives (TV), total variation on both first and second order derivatives (TV+2d), Huber loss penalty on first order derivatives (Huber), Huber loss penalty on first and second order derivatives (Huber+2d), Huber penalty on 1st and 2nd order derivatives combined with BM3D prior [DFKE07] (BM3D), and Huber penalty on 1st and 2nd order derivatives combined with BM3D and cross-channel priors [HRH*13] (BM3D+CC). For the cross-channel prior, we implement it between color channels, as well as between Stokes vector components. We show in Figure 10 the results for

two typical scenarios. The first is a fruit scene with unpolarized indoor illumination (upper part). The second is the cellphonecases scene with polarized illumination (lower part). In each case, we add Gaussian noise with $\sigma = 2$. Among all the priors, Huber penalty on both first and second order derivatives outperforms the other three candidates for all the polarization components. As the results show, the BM3D prior and cross-channel prior, which proved to be effective for color images, are not helpful for color polarization image reconstruction. This indicates that, due to the very different statistics of Stokes vectors compared with conventional color images, Huber penalty on the first and second order derivatives are the most effective priors for polarization images. We also compared with interpolation methods, and all our optimization based methods have better results than the interpolation method. In addition, we run our algorithm throughout our dataset. The average PSNR results are shown in Table 2. To consider different noise levels, we compare the result with noise $\sigma = 2$ and $\sigma = 3$ respectively. The results indicate that our proposed method with Huber penalty on both first and second order derivatives works better than other candidate priors. We also include the results for bilinear interpolation for a baseline comparison. The bilinear interpolation is applied in the four intensity images after color demosaicking.

In the monochromatic case, we divide the dataset scenes into two parts according to the illumination conditions. For the two cases, we use different regularization weights for the priors, but we fix the weights for all the images in the same illumination conditions. This is because in the polarized illumination, the brightness of the four captured intensities under the micro-polarizers could drop or increase drastically for orthogonal polarization angles. In the unpolarized illumination, such variation is much less.

For the performance of our framework, we implemented the method in both a Matlab (CPU) and a CUDA (desktop GPU) version. The CPU implementation of the overall computation cost looks high, however, a short convergence with a good starting point is close to the converged result and provides high-resolution quality and shorter runtime. The GPU version takes about 5.5 seconds per frame, but has further potential for optimization.

5.3. Experimental Results

In real experiments, we use a monochrome polarization camera PHX050S-P and a color polarization camera PHX050S-Q from Lucid Vision Labs. Both polarization sensors are shipped with Sony IMX250MYR CMOS with 2048×2448 pixels. Each pixel size is $3.45\mu m \times 3.45\mu m$. In the monochrome case, each 2×2 pixels are a group. In the color case, every 4×4 pixels form a super pixel to

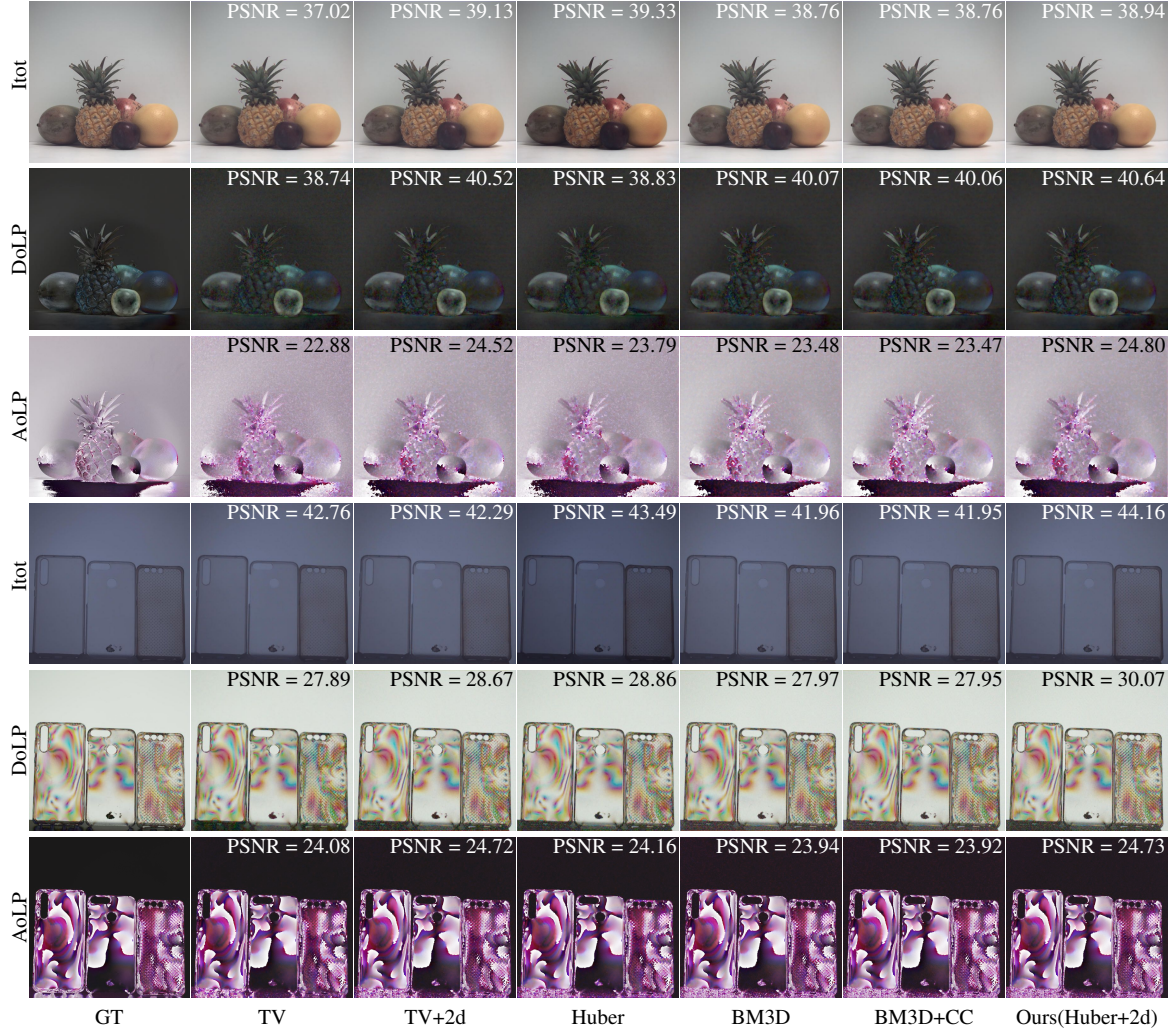


Figure 10: Color polarization demosaicking: A fruit scene with unpolarized illumination, and a cellphone cases scene with polarized illumination. Comparison of optimization based methods with different priors.

Table 2: Average PSNR results for joint color and polarization demosaicking.

Average PSNR		Bilinear	TV	Huber	TV2d	Huber2d +BM3D	Huber2d +BM3D+CC	Ours Huber2d
Unpolarized illumination $\sigma = 2$	Itot	41.52	38.39	40.28	40.32	40.01	40.02	40.18
	DoLP	31.13	32.40	37.22	34.12	37.29	37.28	37.34
	AoLP	18.82	22.23	22.80	22.80	22.39	22.38	24.09
Unpolarized illumination $\sigma = 3$	Itot	40.77	38.01	39.73	39.48	39.80	39.82	39.97
	DoLP	29.58	33.68	36.11	33.65	36.47	36.46	37.03
	AoLP	17.36	20.32	21.51	21.35	21.41	21.40	22.85
Polarized illumination $\sigma = 2$	Itot	44.22	44.18	43.14	44.51	42.75	42.73	44.82
	DoLP	32.68	32.50	32.15	32.74	31.02	30.99	33.64
	AoLP	30.24	30.30	31.00	29.99	28.41	28.39	31.05
Polarized illumination $\sigma = 3$	Itot	43.13	43.02	41.74	43.31	41.76	41.75	43.22
	DoLP	31.14	31.62	30.93	31.67	29.68	29.67	31.75
	AoLP	29.54	29.82	30.22	29.53	27.84	27.84	30.11

sample both polarization and color. We use a Canon EF 50mm f/1.8 II lens operating at the maximum aperture for all the results.

Both color calibration and polarization calibration are necessary before processing. We adopt the method proposed by Akkaynak et al. [ATX^{*}14] to calibrate color correction with a Macbeth color checker. To minimize the influence of polarization, we use unpolarized light for illumination. We find that the Macbeth color checker itself exhibits negligible polarization effects. For simplicity, we only apply white balancing for all the results.

Polarization calibration aims at characterizing the conversion matrix from the Stokes vector to intensities for the micro-polarizers in eachcolor channel. Following the calibration method proposed by York and Gruev [YG12], we mount a high extinction ratio linear polarizer (WP25M-VIS, Thorlabs) on a rotary stage (T-RSW60A, Zaber). A white light source (HPLS245, Thorlabs) is first collimated and then enters the linear polarizer. The exiting light becomes linearly polarized in this way. We rotate the linear polarizer to change the incident angle of polarization. The polarization sensor measures the intensities for different rotation angles. We sweep the rotation angles from 0° to 179° with a 1° step. We take 100 images for each angle and average them to suppress noise. We fit the intensity changing curves and obtain the respective coefficients to construct the conversion matrix.

We show real experimental results in Figure 11 for both monochrome and color polarization cameras with the proposed optimization method. For each camera, we show two arbitrarily captured scenes. Since our method deals with the color/polarization demosaicking simultaneously in an optimization framework, the edges can be handled more properly. This means our method is more conservative such that we do not “create” artificial polarization effects, especially on the boundaries in the scenes.

6. Discussion and Conclusion

Polarization imaging is an effective analytical tool across many disciplines. An improved resolution of polarization imaging is of interest, especially for analyzing internal stress of glass and plastics that are not detectable from conventional imaging approaches. Another crucial application includes highlighting the imperfections and scratches of transparent objects, especially those fabricated from plastic. In order to improve the reconstruction quality of the color and polarization information, we have demonstrated an effective algorithm to combat imperfect issues by inverting the unknown Stokes vectors from a single captured mosaic image within the ADMM framework. The resulting intensity, DoLP, and AoLP outperforms interpolation based methods, and offer more accurate measurements for the high dimensional color polarization information. Our self-constructed high-resolution color polarization image dataset covers as many polarization scenarios as possible that occur in the natural world, offering a large database for algorithm evaluation and polarization analysis. With the aid of our high-resolution color polarized illumination images, the surface scratches, and internal stress characteristics of the objects are quite distinct. We envision the methods presented in this paper will enable many more applications in machine vision, biomedical imaging, remote sensing, marine science, etc. for both research and industry.

Acknowledgements

We are grateful to the best paper committee of VMV 2019 for recommending the original paper [QFWH19] to Computer Graphics Forum, and providing us with an opportunity for presenting this extended work. This work was supported by King Abdullah University of Science and Technology as part of VCC center baseline funding and an equipment donation from LUCID Vision Labs. We thank Dr. Alex Tibbs for sharing data for initial test and Nadya Suvorova for helping dataset construction.

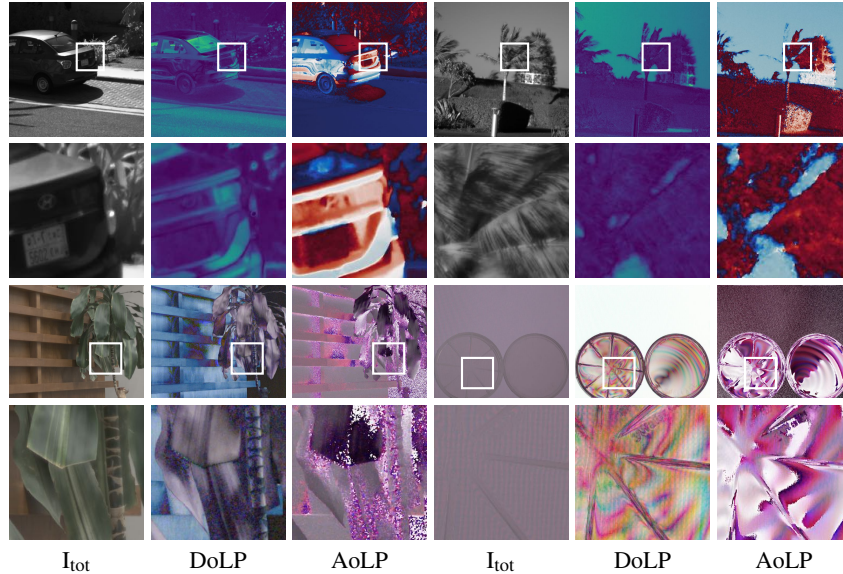


Figure 11: Experimental results for both monochrome (left) and color (right) polarization cameras with the proposed reconstruction algorithm. We show reconstruction results of I_{tot} , DoLP, and AoLP for two arbitrarily captured real scenes.

Appendix A: Müller Matrix

The polarization property of an optical element is characterized by its Müller matrix. In general, the Müller matrix for an ideal linear polarizer oriented θ with respect to horizon is

$$\mathbf{M}_\theta = \frac{1}{2} \begin{bmatrix} 1 & \cos(2\theta) & \sin(2\theta) \\ \cos(2\theta) & \cos^2(2\theta) & \sin(2\theta)\cos(2\theta) \\ \sin(2\theta) & \sin(2\theta)\cos(2\theta) & \sin^2(2\theta) \end{bmatrix}. \quad (18)$$

So the Müller matrices for 0° , 45° , 90° and 135° polarizers are

$$\left\{ \begin{array}{l} \mathbf{M}_0 = \frac{1}{2} \begin{bmatrix} 1 & 1 & 0 \\ 1 & 1 & 0 \\ 0 & 0 & 0 \end{bmatrix}, \quad \mathbf{M}_{90} = \frac{1}{2} \begin{bmatrix} 1 & -1 & 0 \\ -1 & 1 & 0 \\ 0 & 0 & 0 \end{bmatrix}, \\ \mathbf{M}_{45} = \frac{1}{2} \begin{bmatrix} 1 & 0 & 1 \\ 0 & 0 & 0 \\ 1 & 0 & 1 \end{bmatrix}, \quad \mathbf{M}_{135} = \frac{1}{2} \begin{bmatrix} 1 & 0 & -1 \\ 0 & 0 & 0 \\ -1 & 0 & 1 \end{bmatrix}. \end{array} \right. \quad (19)$$

An ideal polarizer can transmit all the light parallel to its orientation angle, and block light completely in the perpendicular direction. In reality, fabrication artifacts lead to imperfections on the polarizer. The parallel and perpendicular transmittance become k_1 and k_2 . Diattenuation is $D = (k_1 + k_2)/(k_1 - k_2)$ and extinction ratio is $ER = k_1/k_2 = (D + 1)/(D - 1)$.

The Müller matrices for the above polarizers are now

$$\left\{ \begin{array}{l} \mathbf{M}_0 = \frac{1}{2} \begin{bmatrix} k_1^0 + k_2^0 & k_1^0 - k_2^0 & 0 \\ k_1^0 - k_2^0 & k_1^0 + k_2^0 & 0 \\ 0 & 0 & 0 \end{bmatrix}, \\ \mathbf{M}_{45} = \frac{1}{2} \begin{bmatrix} k_1^{45} + k_2^{45} & 0 & k_1^{45} - k_2^{45} \\ 0 & 0 & 0 \\ k_1^{45} + k_2^{45} & 0 & k_1^{45} - k_2^{45} \end{bmatrix}, \\ \mathbf{M}_{90} = \frac{1}{2} \begin{bmatrix} k_1^{90} + k_2^{90} & - (k_1^{90} - k_2^{90}) & 0 \\ - (k_1^{90} - k_2^{90}) & k_1^{90} + k_2^{90} & 0 \\ 0 & 0 & 0 \end{bmatrix}, \\ \mathbf{M}_{135} = \frac{1}{2} \begin{bmatrix} k_1^{135} + k_2^{135} & 0 & - (k_1^{135} + k_2^{135}) \\ 0 & 0 & 0 \\ - (k_1^{135} - k_2^{135}) & 0 & k_1^{135} + k_2^{135} \end{bmatrix}. \end{array} \right. \quad (20)$$

Since the sensor can only measure the intensity, for each super pixel in the polarization sensor, the captured intensities for 0° , 45° , 90° and 135° can be obtained from the Stokes vector as follows

$$\begin{bmatrix} I_0 \\ I_{45} \\ I_{90} \\ I_{135} \end{bmatrix} = \frac{1}{2} \begin{bmatrix} 1 & 1 & 0 \\ 1 & 0 & 1 \\ 1 & -1 & 0 \\ 1 & 0 & -1 \end{bmatrix} \begin{bmatrix} S_0 \\ S_1 \\ S_2 \end{bmatrix}. \quad (21)$$

On the other hand, the conversion from the four intensities to Stokes vector can also be written in the matrix-vector product form by

$$\begin{bmatrix} S_0 \\ S_1 \\ S_2 \end{bmatrix} = \begin{bmatrix} 0.5 & 0.5 & 0.5 & 0.5 \\ 1 & 0 & -1 & 0 \\ 0 & 1 & 0 & -1 \end{bmatrix} \begin{bmatrix} I_0 \\ I_{45} \\ I_{90} \\ I_{135} \end{bmatrix}. \quad (22)$$

Appendix B: Calibration

For calibration, we rotate an external polarizer with a high extinction ratio in front of the polarization sensor, and can there-

fore assume the input light is perfectly linearly polarized at a specific angle. The reference frames for the polarizer rotation angle and the sensor polarization angle are usually not the same, and we denote the difference as β . So the Stokes vector for the incident polarized light at rotation angle α is $S_{in} = [1, \cos(2(\alpha + \beta)), \sin(2(\alpha + \beta))]^T$.

Due to fabrication tolerances, the orientation angles for the micropolarizers may be slightly different from their nominal values. The real orientation angle can be expressed as $\theta + \Delta\theta$, where $\Delta\theta$ is the orientation angle error. According to Eq. (21), the intensity received on the sensor is

$$I_\theta = (k_1^\theta + k_2^\theta) + (k_1^\theta - k_2^\theta) \cos(2(\theta + \Delta\theta - \alpha - \beta)). \quad (23)$$

We sweep the rotation angle from 0° to 179° with a 1° step, and observe the intensity changes for the 0° , 45° , 90° and 135° micropolarizers. The curves for each color channel are shown in Figure 12. We fit the curves using the following equation

$$f(\alpha) = a_0 + a_1 \cos(2(\theta - \alpha - \beta)). \quad (24)$$

The unknown value of β is part of the fitting process. $\Delta\theta$ is then calculated as $\Delta\theta = \theta - \bar{\beta}$. The final the calibration matrices for our polarization camera are as follows:

$$\begin{aligned} \mathbf{P}_r &= \begin{bmatrix} 0.4957 & 0.4965 & -0.0011 \\ 0.5073 & 0.0041 & 0.5084 \\ 0.4936 & -0.4939 & 0.0007 \\ 0.5032 & 0.0040 & -0.5026 \end{bmatrix}, \\ \mathbf{P}_g &= \begin{bmatrix} 0.4947 & 0.4937 & -0.0026 \\ 0.5078 & 0.0034 & 0.5065 \\ 0.4925 & -0.4908 & -0.0029 \\ 0.5047 & 0.0029 & -0.5051 \end{bmatrix}, \\ \mathbf{P}_b &= \begin{bmatrix} 0.4924 & 0.4932 & -0.0037 \\ 0.5082 & 0.0045 & 0.5075 \\ 0.4906 & -0.4890 & -0.0049 \\ 0.5083 & 0.0044 & -0.5114 \end{bmatrix}. \end{aligned}$$

References

- [AK02] ANDREOU A. G., KALAYJIAN Z. K.: Polarization imaging: principles and integrated polarimeters. *IEEE Sensors Journal* 2, 6 (2002), 566–576. 1
- [ATX*14] AKKAYNAK D., TREIBITZ T., XIAO B., GÜRKAN U. A., ALLEN J. J., DEMIRCI U., HANLON R. T.: Use of commercial off-the-shelf digital cameras for scientific data acquisition and scene-specific color calibration. *JOSA A* 31, 2 (2014), 312–321. 10
- [DFKE07] DABOV K., FOI A., KATKOVNIK V., EGIAZARIAN K.: Image denoising by sparse 3-D transform-domain collaborative filtering. *IEEE Transactions on image processing* 16, 8 (2007), 2080–2095. 3, 8
- [GDB*18] GARCIA M., DAVIS T., BLAIR S., CUI N., GRUEV V.: Bioinspired polarization imager with high dynamic range. *Optica* 5, 10 (2018), 1240–1246. 2
- [GEM*17] GARCIA M., EDMISTON C., MARINOV R., VAIL A., GRUEV V.: Bio-inspired color-polarization imager for real-time in situ imaging. *Optica* 4, 10 (2017), 1263–1271. 2
- [GG11] GAO S., GRUEV V.: Bilinear and bicubic interpolation methods for division of focal plane polarimeters. *Opt. Express* 19, 27 (2011), 26161–26173. 2, 6
- [HMB*14] HSU W.-L., MYHRE G., BALAKRISHNAN K., BROCK N., IBN-ELHAJ M., PAU S.: Full-stokes imaging polarimeter using an array of elliptical polarizer. *Opt. Express* 22, 3 (2014), 3063–3074. 2

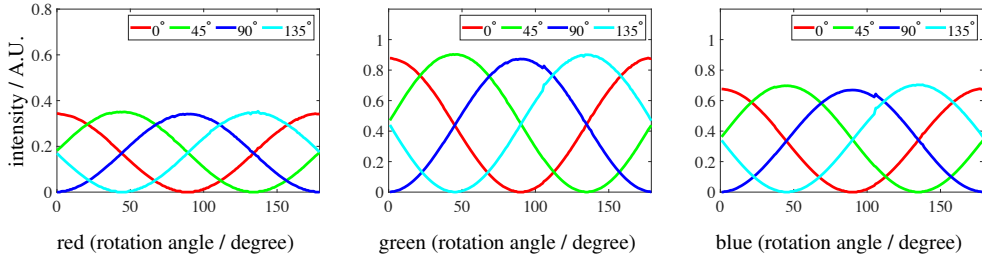


Figure 12: Polarization calibration. Intensity changing curves are measured for 0° , 45° , 90° and 135° in each color channel.

- [Hor14] HORVÁTH G.: *Polarized light and polarization vision in animal sciences*, vol. 2. Springer, 2014. 1
- [HRH*13] HEIDE F., ROUF M., HULLIN M. B., LABITZKE B., HEIDRICH W., KOLB A.: High-quality computational imaging through simple lenses. *ACM Transactions on Graphics (TOG)* 32, 5 (2013), 149. 3, 8
- [HST*14] HEIDE F., STEINBERGER M., TSAI Y.-T., ROUF M., PAJAK D., REDDY D., GALLO O., LIU J., HEIDRICH W., EGIAZARIAN K., ET AL.: FlexISP: A flexible camera image processing framework. *ACM Transactions on Graphics (TOG)* 33, 6 (2014), 231. 3
- [Hub64] HUBER P. J.: Robust estimation of a location parameter. *Ann. Math. Statist.* 35, 1 (1964), 73–101. 3
- [LGFB18] LAPRAY P.-J., GENDRE L., FOULONNEAU A., BIGUÉ L.: Database of polarimetric and multispectral images in the visible and nir regions. In *Proceedings of the Unconventional Optical Imaging* (2018), vol. 10677, SPIE, p. 1067738. 4
- [LZPK19] LI N., ZHAO Y., PAN Q., KONG S. G.: Demosaicing dofp images using newton's polynomial interpolation and polarization difference model. *Optics Express* 27, 2 (2019), 1376–1391. 2, 6, 7, 8
- [MLB18] MIHOUBI S., LAPRAY P.-J., BIGUÉ L.: Survey of demosaicking methods for polarization filter array images. *Sensors* 18, 11 (2018), 3688. 6
- [QFWH19] QIU S., FU Q., WANG C., HEIDRICH W.: Polarization Demosaicing for Monochrome and Color Polarization Focal Plane Arrays. In *Proceedings of the Vision, Modeling and Visualization* (2019), Schulz H.-J., Teschner M., Wimmer M., (Eds.), The Eurographics Association. doi:10.2312/vmv.20191325. 2, 10
- [TDBR17] TIBBS A., DALY I., BULL D., ROBERTS N.: Noise creates polarization artefacts. *Bioinspiration & biomimetics* 13, 1 (2017), 015005. 2
- [TDRB18] TIBBS A. B., DALY I. M., ROBERTS N. W., BULL D. R.: Denoising imaging polarimetry by adapted BM3D method. *JOSA A* 35, 4 (2018), 690–701. 2, 4, 7
- [TGCS06] TYO J. S., GOLDSTEIN D. L., CHENAULT D. B., SHAW J. A.: Review of passive imaging polarimetry for remote sensing applications. *Appl. Opt.* 45, 22 (2006), 5453–5469. 1
- [TLR09] TYO J. S., LACASSE C. F., RATLIFF B. M.: Total elimination of sampling errors in polarization imagery obtained with integrated microgrid polarimeters. *Opt. Lett* 34, 20 (2009), 3187–3189. 2, 6, 7
- [YG12] YORK T., GRUEV V.: Characterization of a visible spectrum division-of-focal-plane polarimeter. *Appl. Opt.* 51, 22 (2012), 5392–5400. 10
- [YMU*16] YAMAZAKI T., MARUYAMA Y., UESAKA Y., NAKAMURA M., MATOBA Y., TERADA T., KOMORI K., OHBA Y., ARAKAWA S., HIRASAWA Y., ET AL.: Four-directional pixel-wise polarization CMOS image sensor using air-gap wire grid on $2.5\text{-}\mu\text{m}$ back-illuminated pixels. In *Proceedings of the IEEE International Electron Devices Meeting (IEDM)* (2016), IEEE, pp. 8–7. 2
- [ZLHC16] ZHANG J., LUO H., HUI B., CHANG Z.: Image interpolation for division of focal plane polarimeters with intensity correlation. *Opt. Express* 24, 18 (2016), 20799–20807. 2, 6, 7
- [ZLL*18] ZHANG J., LUO H., LIANG R., AHMED A., ZHANG X., HUI B., CHANG Z.: Sparse representation-based demosaicing method for microgrid polarimeter imagery. *Optics letters* 43, 14 (2018), 3265–3268. 2, 6, 7
- [ZLZY19] ZENG X., LUO Y., ZHAO X., YE W.: An end-to-end fully-convolutional neural network for division of focal plane sensors to reconstruct s 0, dolp, and aop. *Optics express* 27, 6 (2019), 8566–8577. 2, 6, 7, 8